11

Novel Computational Approaches for Understanding Computed Tomography (CT) Images and Their Applications

Oyeon Kum
School of Electronics Engineering, Kyungbook National University, Daegu
Korea

1. Introduction

We discuss three closely relevant computational approaches for understanding computed tomography (CT) images: X-ray imaging, medical image analysis, and the application of radiotherapy planning. The computational approaches have been widely used in X-ray research for more than three decades (Colijn, 2004; Feldkamp et al., 1984; Ju et al., 2010; Kak, 1999; Kum, 2010; KumPark, 2010; Kum, 2007; 2005; Kim, 2006; Kum et al., 2009; Peterzol et al., 2008). To understand CT images is to understand photon and/or electron scattering in matter, which can easily be done by the Monte Carlo method. Our research is mostly based on our in-house Monte Carlo code, PMCEPT code, which was developed recently (Ju et al., 2010; Kum, 2007; 2005; Kim, 2006; Kum et al., 2009; Peterzol et al., 2008).

Image processing to delineate tumor and to extract body contours and organ boundaries for dosimetric modeling in radiotherapy planning has become a routine process since CT scanners became available in the late 1970s (Gu et al., 2006; Haris et al., 1998; Kum et al., 2007; Kim et al., 2007; Kum, 2007; Kum et al., 2008). Moreover, pixel by pixel dose computation for planning is performed on the bulk inhomogeneous human body via the CT image. Recently, almost all major treatment machine manufacturers have been influenced by these technically advanced attributes to mount a cone beam CT(CBCT) 3D-imaging system on their linear accelerators for radiotherapy (Moore et al., 2006). They are using flat panel transducers to acquire a rotation fluoroscopy image sequence for input to 3D filtered back-projection algorithms. However, the development of cone beam tomography for radiotherapy is far from complete, with X-ray source, image transducer, reconstruction algorithms, and techniques for image profile collection still being researched (Feldkamp et al., 1984; Kak, 1999; Lagravere et al., 2008; Miceli et al., 2007; Wang et al., 1993; Zhao et al., 2009).

Simulation is a helpful tool to develop and optimize a new CBCT imaging system and to understand the influence of the various adjustable parameters. It acts as a virtual experimental workbench to offer powerful means for choosing the most suitable components and for predicting the future imaging system performance. It may enable the behavior of the whole imaging system to be investigated in complex situations by using simulated images which can be obtained in little time and at low cost (Colijn, 2004; Duvauchelle et al., 2000; Freud et al., 2006; 2004; Li et al., 2008; Miceli et al., 2007).

Although Monte-Carlo simulation is a powerful method for the investigation of the production of scattered particles in a medium in detail, deterministic calculations based on ray tracing algorithms are known as a powerful alternative to the Monte Carlo approaches to simulate X-ray imaging system whenever computation time is a critical issue (Freud et al., 2006; 2004). We focus on a simpler ray tracing approach in this chapter to describe our X-ray imaging system.

One of the important issues in medical imaging is to precisely segment structures of interest from a huge dataset, accurately represent them, efficiently visualize them, and perform measurements appropriate for diagnosis and therapy guidance, or other applications (Gu et al., 2006; Haris et al., 1998; Jos, 2001; Lagravere et al., 2008; Moga et al., 1998; Vincent, 1991). Advances in the area of computer science have a tremendous impact on the interpretation of medical images. Computer Aided Diagnosis systems aim to provide computer output as a second opinion in order to assist physicians in the detection of abnormalities, quantification of disease progress, and differential diagnosis of lesions, which enhances the physicians' capabilities and reduces the time required for accurate diagnosis.

Image segmentation is the process of dividing images into regions according to its characteristics involved in the images. The segmented objects are in the form of images that are more meaningful, easier to understand, and easier to analyze. In order to locate objects and boundaries in images, either data-based methods or pixel classification methods are used. Data-based approaches involve mathematical morphology, model-fitting, level-set methods, thresholding, edge-detection, and knowledge-based classification. Pixel classification techniques have used neural networks, Markov random field modeling, and active contours. The simplest idea for segmenting CT images is to classify the Hounsfield units (CT numbers) of the DICOM file into clusters. Intuitively, the Hounsfield unit of a pixel is interpreted as its altitude in the relief of each cluster, which leads to the watershed image segmentation algorithm. We discuss this algorithm in this chapter to provide semi-automatic segmentation of CT image, including the pre- and post-processing procedures for alleviating the drawbacks of a pure watershed algorithm.

Images are digitally processed to maximize the perception of medically important features. Physically meaningful Hounsfield values (CT numbers) in the computer memory are adjusted to suit grey values on a display monitor for the special application requirements. The customized radiation therapy applications are easily available with the information of the clustered Hounsfield values segmented by the watershed algorithms. The physico-chemical information from each patient's CT image such as the mass density and the chemical elements' weights of atomic compositions in each voxel corresponding to each pixel of the CT image is extracted via segmentation process because the Hounsfield unit includes quantitative information about the radiological properties of the different tissues (Lagravere et al., 2008; Scheneider et al., 2000). Tissue inhomogeneities are expressed in terms of different Hounsfield values, which makes the corrected dose calculations available for inhomogeneous target materials such as human body.

Exact estimate of clinical dose distribution in a patient body is the ultimate goal for the radiotherapy treatment planning (Moore et al., 2006). The exact dose calculation can be done by direct simulation of the interactions between the radiation and the patient tissue, the mass density and the chemical composition of the tissues, with Monte Carlo code such as PMCEPT code (Kum, 2007; 2005). With the advances of the computing power, applications of the Monte Carlo method for patient dose calculations have recently become more and more common by using the patient's CT images. Since this idea is closely correlated to the Hounsfield

values, radiotherapy treatment planning is closely relevant to the CT imaging techniques, reconstruction algorithms, and segmentation algorithms in the computer simulations.
In this context, our laboratory initiated a comprehensive simulation research program of "from CT imaging to radiotherapy treatment planning with the state of the art information technologies." The major subject of this research program is to use our in-house Monte Carlo code, PMCEPT code to simulate directly the interactions between the radiation and the patient body. However, for better understanding of the complex physical phenomena involved in the radiation interactions with matter, this program involves closely relevant augmented novel computational approaches for each phase which are introduced in this chapter in order better to understand the CT images.

2. Cone beam computer tomography simulator

2.1 Virtual cone beam imaging technique

The major advantages of cone-beam acquisition are the reduction of data collection time and lower patient absorbed dose per scan. This is particularly important for real-time imaging of moving structures such as the beating heart, or the use of image guided radiotherapy treatment (IGRT) (Moore et al., 2006). With the advances in planar detector technology, it is expected that next generation scanners will adopt the cone beam geometry. This is the reason we developed a CBCT simulator in our laboratory.
CT image is acquired by the physical principle that the X-ray interacts with the body's tissues while it is passing through the body. If it does not experience some type of interaction, such as absorption, attenuation, and scattering with the body, the detected signal would not contain any useful information regarding the internal anatomy, and thus it would not be possible to construct an image of the anatomy with the detected information (Kum, 2010).
Although a medical image has an aesthetic appearance, the acquisition of an image is closely related to both the technical quality of the image and the adjustment of the input parameters. Thus, image quality in medical imaging involves very little artistic evaluation but a great deal of technical appraisal. For example, better CT images can be obtained when the radiation dose to the patient is high. However, patient safety and comfort must be considered first while acquiring medical images. Consequently, excessive patient dose in the pursuit of a perfect image is not acceptable, rather, a power balance is required to satisfy both the patient safety and image quality.
The procedure involved in obtaining CT image is that the patient remains stationary on the examination table while the X-ray tube rotates in a circular orbit around the patient in a plane perpendicular to the length-axis of the patient. The data acquired from the detectors are fed in to a computer which, after numerous calculations, produces a tomogram of the patient, i.e., a map of linear attenuation coefficients whose value is assigned a grey scale value on the display-monitor and is presented in a square picture element (pixel) of the image. In the 2D tomography, after a complete rotation of X-ray tube, the table with the patient is moved a small distance and the next slice can be measured. Thus, it takes a comparatively long time and gives high dose to the patient. Moreover, it is not possible to obtain, in particular, real-time imaging of moving structures, such as the beating heart, or contrast agent flow through the body in 2D fan beam CT imaging.
CBCT is a three-dimensional extension of two dimensional fan beam tomography. X-rays diverging as a cone from the source irradiates on the body, and data corresponding to passing X-rays is recorded on a planar detector surface (receptors) (Freud et al., 2006; 2004). Such cone beam projections are collected for a multitude of source positions along a source orbit which

may be a complete circle or not. The main advantages of cone beam acquisition system are the reduction of data collection time, reduced dose to the patient, and real-time imaging of moving structures. High quality CBCT images may be generated with high patient exposures and a large number of X-ray image profiles for reconstruction. However, this is not practical in view of the general regulations that embodies the principle of doses being "as low as reasonably practical" in the context of risks and benefits to the patient. Thus, there still remain many important research problems in CBCT imaging technology (Moore et al., 2006).

The apparent drawback of the CBCT image is the significant degradation of image quality due to the contamination of X-ray projection data with scattered photons and/or secondary electrons, resulting in a decrease of low-contrast detectability, cupping artifacts and streak artifacts between different objects (Peterzol et al., 2008). The amount of scatter contamination depends strongly on the type of imaging and detector geometry used as well as the object under study. Monte Carlo methods are known to be the best to accurately simulate scatter in X-ray imaging. Our in-house Monte Carlo code, PMCEPT code, has a capability to simulate the photon energy as low as 1 KeV and as high as 1 GeV against the targets of about hundred chemical elements, their compositions, and mixtures (KumPark, 2010; Kum, 2005). However, when low noise scatter projections have to be simulated, these Monte Carlo simulations tend to be very time consuming even though we use high performance parallel computing (Kim, 2006). Thus, it is worthwhile to add the most simplified approach to simulate CBCT X-ray projection by using ray tracing algorithms which is discussed in detail in the following.

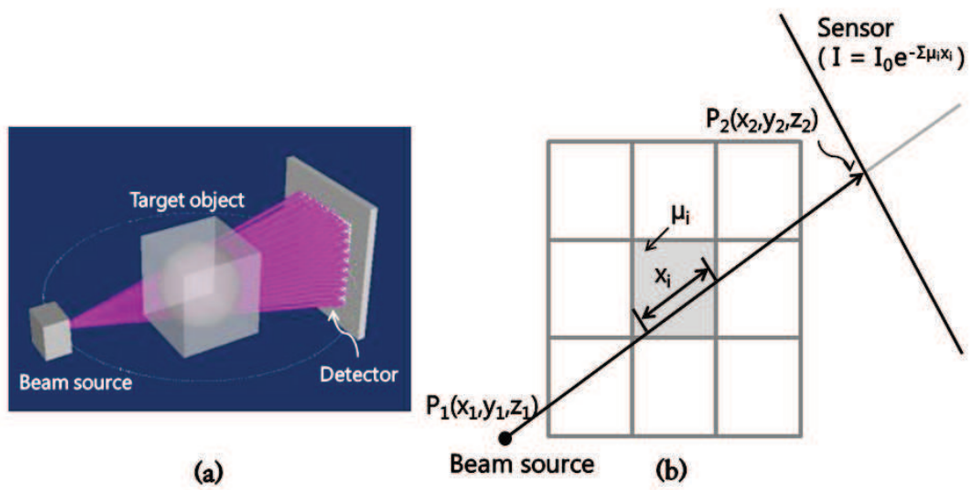

Fig. 1. Cone beam simulator model. (a) A set of ray beams is emitted towards every pixel center of the detector. (b) Radiological path is determined by summing up the length times the corresponding attenuation value.

Cone beam X-ray projector can be modeled with a bunch of rays that are emitted by a source point towards irradiated objects. This is the simplest and fastest in algorithm speed but the scattering effects and quantum noise are not taken into account. A plane panel detector is described by the grid of pixels with perfect quantum efficiency in a 3D scene. The right-handed Cartesian coordinate system is appropriate to describe the position and orientation of the source, object, and detector in the three dimensions. As shown in Fig. 1 (a), from the X-ray source, a set of ray beams is emitted towards every pixel center of the detector. The exact radiological path through the phantom volume is calculated on the basis

of the calculation of ray-box intersection (see Fig. 1 (b)) because the phantom volume makes up the grid of cuboid cells (meshes or voxels). Determining the total path length with a cuboid grid is simpler than it is with a triangulated surface model. Radiological path is determined by summing up the length times the corresponding attenuation coefficient of the ray segments that cut each cell together along the ray path (see Fig. 1 (b)). There are many algorithms to calculate the exact radiological path through the phantom volume. Among them, our system adopted the well-known Siddon's fast or improved algorithms (Siddon, 1985). Our code was purposefully developed from scratch (no recourse to existing 'black-box' code libraries), including specifically designed and optimized ray casting algorithms.

The X-ray attenuation law, together with ray tracing techniques forms the basis of our code. The detector measures the attenuation in the phantom volume along the path of a particular ray. The attenuation of X-rays with a typical mean energy of 50–150 keV is determined by three different physical processes; Compton scattering (σ^{com}), photoelectric absorption (σ^{pho}), and Rayleigh scattering (σ^{ray}). The particle fluence of the transmitted X-rays entering the detector behind the phantom (Kum, 2010) is

$$\Phi(E) = \Phi_o(E) exp(-\int_0^l \mu(E,s)ds), \tag{1}$$

where $\Phi_o(E)$ is the initial particle fluence of the X-rays and $\mu(E,s)$ is the linear attenuation coefficient of the phantom material at position s and energy E. The attenuation coefficient depends on the atomic compositions at point s,

$$\mu(E) = \rho N_A \sum_{i=1}^{n} (\frac{w_i}{A_i}\sigma_i(E)), \tag{2}$$

where ρ is overall mass density (g/cm^3) at point s, N_A the Avogadro constant, i the element index, w_i the element weight, A_i the atomic mass (g/mol), and σ_i the total cross section, $\sigma_i^{com} + \sigma_i^{pho} + \sigma_i^{ray}$. The corresponding attenuation coefficients, associated with any elementary or compound substance, can be obtained from available databases, such as EPDL97 (Cullen et al., 1997).

The measured detector signal is either proportional to the particle fluence (i.e. energy fluence) or, to the energy deposition per mass if the detector is an ionization chamber. In general, projection value r which is calculated as the logarithmic ratio of the signal measured without a phantom (Φ_o) in the CT scanner and the signal of the X-rays attenuated by the phantom (Φ_E), i.e. $r = ln(\Phi_o/\Phi_E)$. In the case of monochromatic X-rays, we have:

$$r = ln(\frac{\Phi_o}{\Phi_E}) = \int_0^l \mu(E,s)ds \equiv \sum \mu(E,s_i)\Delta s, \tag{3}$$

where the sum runs from 0 to l. Reconstructing these line integrals would give the values $\mu(E)$ of the different material, i.e. a well defined physical quantity.

Although most commercial CT scanners produce more or less polychromatic X-rays, even though the bandwidth is not so broad, we only use the monochromatic X-rays in this simpler ray casting model, which is different from the full Monte Carlo model. Thus, we neglect the unavoidable beam hardening effect with polychromatic X-rays in this model. However, we consider the different CT scanner effect of having wide range of measured attenuation values. We obtain comparable attenuation values for different CT scanners by rescaling them with respect to that of water because most soft tissues have linear attenuation coefficients very

similar to that of water over a large photon energy interval. The CT number or Hounsfield value (H) is defined as follows:

$$H = 1000(\frac{\mu}{\mu_{H_2O}} - 1) \tag{4}$$

where μ_{H_2O} is the mean attenuation coefficient of water. Thus, water has always the value 0 and air the value -1000. Note that the ratio of (μ/μ_{H_2O}) depends slightly on the spectral function $\hat{f}(E)$ of the commercial CT scanner, and therefore the CT number is a scanner-dependent quantity with fixed values for water and air (Scheneider et al., 2000).

These investigations show that we can also define uniquely patient body's mass density and chemical composition according to the Hounsfield values of the patient's CT data. Thus, we emphasize that the process of clustering pixels in a medical image dataset according to Hounsfield values classifies anatomical structures with corresponding physiological properties. This classification has a wide variety of applications in medical research and visualization, i.e. computer-aided diagnosis and radiotherapy treatment planning. Therefore, these three areas are closely relevant (KumPark, 2010).

A straightforward ray tracing technique would require computing time that scales with the array size N^3. Siddon (Siddon, 1985) proposed a fast method to trace the rays whose computing time scales with 3N. In this study, a refinement to Siddon's algorithm is investigated. Our new algorithm uses an incremental or decrement operation for computing the voxel indeces which improves computing time a little bit. Moreover, like the PMCEPT Monte Carlo code, ray tracing algorithm uses MPI based parallel computing algorithm for the projection angle on a Linux PC cluster. It is very efficient parallel algorithm because there is no intercommunication between nodes while computing. The final project data in the form of 'RAW' file is used for reconstruction, which is discussed in the following.

The two kinds of algorithm, ray tracing and Monte Carlo are not exclusive, but complementary. The Monte Carlo approach is slow but correct. Several hours or even days may be needed to get an image with an acceptable noise level (e.g. 1%), but it incorporates all the photon-material interactions into account, such as scattering, fluorescence, and electron processes. The ray tracing approach is fast and does not produce any noise. To simulate realistic images, a few statistical noise models in each photon energy channel can be added. A full sinogram can be simulated from computer-aided design (CAD) models in a few minutes using a current computer for the directly transmitted photons. This ray tracing with CAD model is also closely related to the optimization simulation used for the optimized radiotherapy planning.

2.2 Reconstruction technique

A reconstruction algorithm is a mathematical method to find the attenuation coefficients, μ-values, in each voxel based on all the measured data in the projection profiles. The procedure to reconstruct the image, based on the many projections at different angles, is performed with a reconstruction algorithm. Several types of reconstruction algorithms are available: filtered backprojection, direct Fourier, and algebraic reconstruction techniques. For the acquisition geometry of circular rotation of a cone about a fixed iso-center, Feldkamp, Davis, and Kress (FDK) algorithm (Feldkamp et al., 1984; Kak, 1999) which uses weighted filtered back-projection is used most often in practice, although it is an approximate method. Specifically, this algorithm is appropriate for the incomplete data set which is prone to inherent artifacts, in particular, away from the source plane.

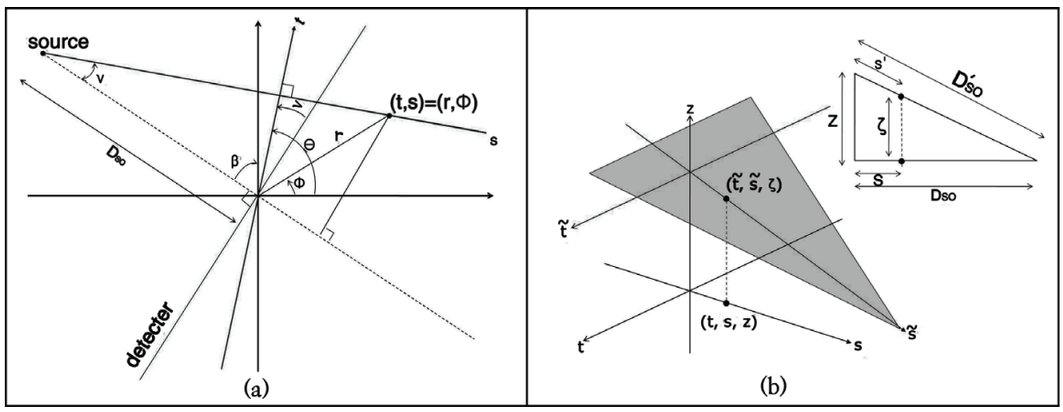

Fig. 2. Geometry of cone beam reconstruction. (a) Fan beam reconstruction geometry corresponding to the mid-plane of cone beam. (b) Tilted fan geometry of FDK algorithm.

Figure 2(a) shows mid-plane geometry of cone beam tomography (equivalent to fan beam reconstruction geometry or 2D parallel projection), and (b) shows tilted fan geometry of FDK algorithm. Three dimensional Radon transformation delivers integration values over planes formed by the detector plane, rather than along lines (formed by the receptors). The cone beam reconstruction algorithm is driven from the fan beam reconstruction algorithm (mid-plane geometry of cone beam) for the point (t, s) which represents the 2D parallel projection.

$$g(t,s) = \frac{1}{2}\int_0^{2\pi} \frac{D_{SO}^2}{(D_{SO}-s)^2} \int_{-\infty}^{\infty} R_\beta(p) f\left(\frac{D_{SO}t}{D_{SO}-s} - p\right) \frac{D_{SO}}{\sqrt{D_{SO}^2+p^2}} dp d\beta. \tag{5}$$

where,

$$t = x\cos\beta + y\sin\beta, \tag{6}$$

$$s = -x\sin\beta + y\cos\beta, \tag{7}$$

$$x = r\cos\phi, \tag{8}$$

$$y = r\sin\phi. \tag{9}$$

$R_\beta(p)$ represents the 2D projection data, p describes a linear detector array intersecting the origin of the reconstruction coordinate system, D_{SO} denotes the (source) distance between the X-ray source and the origin of the reconstruction coordinate system, and $f(\cdot)$ is the reconstruction filter defined as Kak and Slaney (Kak, 1999),

$$f(p) = \int_{-W}^{W} \mid \omega \mid \exp(j\omega p) d\omega. \tag{10}$$

In a cone beam reconstruction, all the fans except the mid plane are tilted out of the plane of rotation so that the size of the fan and the coordinate system of the reconstructed point change. Thus, a new coordinate system $(\tilde{t}, \tilde{s})$ is defined that represents the location of the reconstructed point with respect to the tilted fan shown in Fig. 2(b). Because the geometry of the fan size changes, both the source-to-origin distance, D_{SO}, and the angular differential, β, are changed. The new source-to-origin distance is given by

$$D_{SO}'^2 = D_{SO}^2 + \zeta^2, \tag{11}$$

where ζ is the height of the fan above the center of the plane of rotation. In addition, for the tilted fan the increment of angular rotation $d\beta'$ must be,

$$D_{SO}d\beta = D'_{SO}d\beta' \Rightarrow d\beta' = \frac{D_{SO}d\beta}{\sqrt{D_{SO}^2 + \zeta^2}}. \tag{12}$$

If we replace the 2D reconstruction variables, D_{SO} and β, by the 3D reconstruction variables, D'_{SO} and β', respectively, Eq. 5 becomes

$$g(\tilde{t},\tilde{s}) = \frac{1}{2}\int_0^{2\pi} \frac{D'^2_{SO}}{(D'_{SO}-\tilde{s})^2}\int_{-\infty}^{\infty} R_{\beta'}(p,\zeta) f\left(\frac{D'_{SO}\tilde{t}}{D'_{SO}-\tilde{s}} - p\right)\frac{D'_{SO}}{\sqrt{D'^2_{SO}+p^2}}dpd\beta'. \tag{13}$$

To return the reconstruction to the original orthogonal (t,s,z) coordinate system we replace the 3D reconstruction variables D'_{SO} and β', by the 2D rotating plane variables, D_{SO} and β, respectively, in Eq. 13 by using a coordinate transformation,

$$g(t,s,z) = \frac{1}{2}\int_0^{2\pi} \frac{D_{SO}^2}{(D_{SO}-s)^2}\int_{-\infty}^{\infty} R_\beta\left(p, \frac{D_{SO}z}{D_{SO}-s}\right) f\left(\frac{D_{SO}t}{D_{SO}-s} - p\right)\frac{D_{SO}}{\sqrt{D_{SO}^2+p^2+\zeta^2}}dpd\beta, \tag{14}$$

where a coordinate transform is,

$$\tilde{t} = t, \quad \frac{\tilde{s}}{D'_{SO}} = \frac{s}{D_{SO}}, \quad \frac{\zeta}{D_{SO}} = \frac{z}{D_{SO}-s}. \tag{15}$$

In the numerical algorithm the final formula $g(t,s,z)$ in Eq. 14 is usually converted again into $g(x,y,z)$ in the usual 3D Cartesian coordinate system by using the inverse coordinate transformations of Eqs. 6-9. The Eq. 14 is called the generalized Feldkamp's cone beam reconstruction formula. The important problem in the reconstruction algorithm is to choose the reconstruction filter $f(\cdot)$. We assume that the projection data are sampled with a sampling interval of τ cm. If there is no aliasing, this means that in the Fourier domain the projections don't contain any energy outside the frequency interval $(-W,W)$ where

$$W = \frac{1}{2\tau}\text{cycles/cm}. \tag{16}$$

Since the highest frequency of the projections is finite, we have

$$\int_{-\infty}^{\infty} R'_\beta(w,\zeta) \mid w \mid \exp(j2\pi wt)dw = \int_{-\infty}^{\infty} R'_\beta(w,\zeta)F(w)\exp(j2\pi wt)dw, \tag{17}$$

where $R'_\beta(w,\zeta)$ is the one-dimensional Fourier transform of $R_\beta(p,\zeta)$ with respect to p,

$$F(w) = \mid w \mid b_W(w). \tag{18}$$

and

$$b_w(w) = \begin{cases} 1, & \mid w \mid < W \\ 0, & \text{otherwise.} \end{cases} \tag{19}$$

$F(w)$ represents the transfer function of a filter with which the projections must be processed. Thus, the impulse function, $f(t)$, of this filter is given by the inverse Fourier transform of $F(w)$ and is

$$f(t) = \int_{-\infty}^{\infty} F(w)\exp(+j2\pi wt)dw \tag{20}$$

$$= \frac{1}{2\tau^2}\frac{\sin(2\pi t)/2\tau}{2\pi t/2\tau} - \frac{1}{4\tau^2}\left(\frac{sin(\pi t)/2\tau}{\pi t/2\tau}\right)^2, \tag{21}$$

where Eq.16 is used. Since the sampling interval of the projection data is τ, the impulse response, $f(t)$, needs only to be known with the same sampling interval for the digital processing. The samples are given by

$$f(n\tau) = \begin{cases} 0 & n: \text{ even} \\ \frac{1}{4\tau^2} & n = 0 \\ -\frac{1}{n^2\pi^2\tau^2} & n: \text{ odd.} \end{cases} \tag{22}$$

The cone beam reconstruction algorithm can be formulated as three steps:
Step 1: Calculate the pre-weighted projection data,

$$R'_\beta(p,\zeta) = \frac{D_{SO}}{\sqrt{D_{SO}^2 + p^2 + \zeta^2}} R_\beta(p,\zeta). \tag{23}$$

Step 2: Convolve the weighted projection $R'_\beta(p,\zeta)$ with $f(p)/2$ by multiplying their Fourier transforms with respect to p,

$$Q_\beta(p,\zeta) \equiv R'_\beta(p,\zeta) * \frac{1}{2}f(p). \tag{24}$$

Note that this convolution is done independently for each elevation, ζ.
Step 3: Back-project over the three-dimensional reconstruction grid,

$$g(t,s,z) = \int_0^{2\pi} \frac{D_{SO}^2}{(D_{SO}-s)^2} Q_\beta\left(\frac{D_{SO}t}{D_{SO}-s}, \frac{D_{SO}z}{D_{SO}-s}\right) d\beta. \tag{25}$$

The two arguments of the convolved projection, Q_β, represent the transformation of a point in the object into the coordinate system of the tilted fan shown in Fig. 2(b). Note that the cone beam system can not correctly reconstruct the whole object because the beam projection region is a sphere of radius $D_{SO}\sin(\Gamma_m)$, where Γ_m is half the beamwidth angle of the cone and some points outside this region may not be included in any of the projections (Lagravere et al., 2008; Wang et al., 1993).
For the fast ray-tracing, a target object is, in general, included in the smallest cuboid which includes the object, and the cuboid is divided into the same size of small voxels as shown in cylindrical object in Fig. 3(a). Radiological path is calculated by multiplying the attenuation coefficients of the target materials. The void voxels have zero attenuation values (vacuum) and automatically subtracted from the radiological path as shown in Fig.3(b), top-view of the cylindrical object. Thus, there may exist negligible error for the curved objects. In this example, the height of the target cylinder is 160 mm and is divided into 64 slices, so that each slice is 2.5 mm in thickness. The number of pixels in each slice is 512×512 and the width between the pixels is 0.5 mm. 720 projections were simulated for the evenly divided

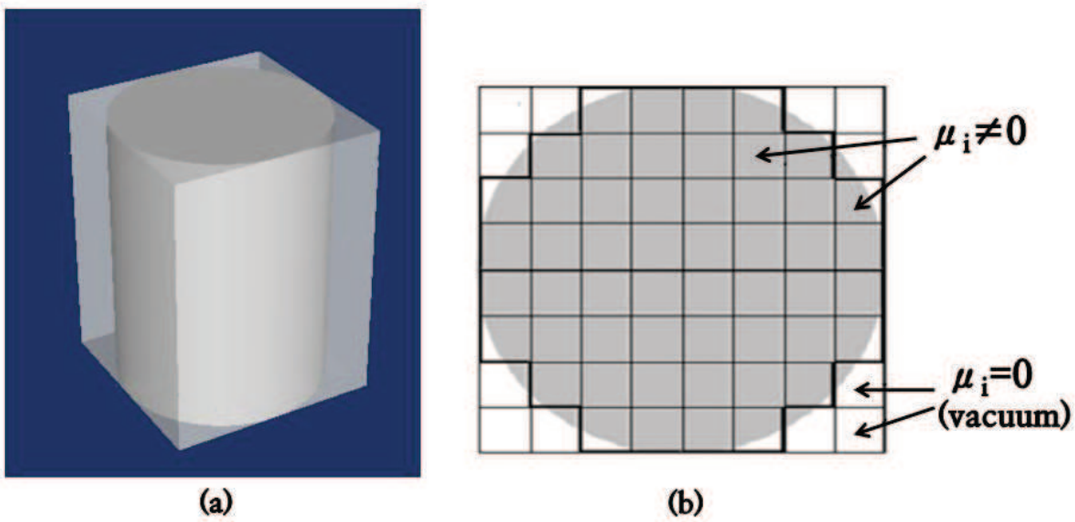

Fig. 3. CAD description of target object. (a) Cylinder object included in cuboid. (b) Top-view of the cylindrical object.

angles. On the plane of rotation (z = 0) the cone beam algorithm is identical to a equi-spatial fan beam algorithm, as discussed above, and the quality of the reconstruction varies with the elevation of the plane because farther from the central plane each point in the reconstruction is irradiated from all directions but now at an oblique angle. Figure. 4 shows reconstruction at z=15 mm, the sixth slice above from the plane of rotation. However, as shown in Fig. 4, there is no noticeable degradation in the reconstruction in our algorithm.

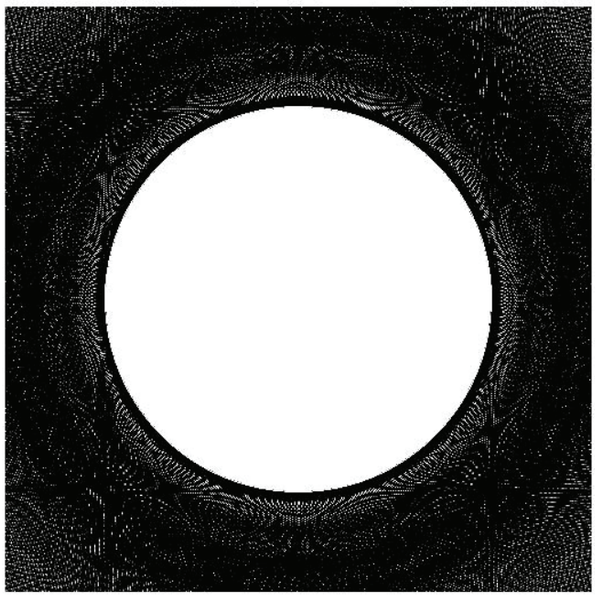

Fig. 4. Reconstructed image (512×512) of the slice at z=15 mm above the rotational plane.

3. Image segmentation

3.1 Watershed segmentation algorithm

Image segmentation is one of the most important issues in computer aided medical imaging. It is now frequently used in the analysis and diagnosis of numerous applications, such as the study of anatomical structure, localization of pathology, treatment planning, and computer-assisted surgery. Computers are indispensable for the analysis of large amounts of data, for tasks that require complex computation, or for the extraction of quantitative information. There are two important reasons for the use of computer aided segmentation: one is to improve upon the conventional expert (human)-based segmentation, and the other is to acquire segmentation prior to visualization or quantification for the analysis of medical images (Gu et al., 2006; Haris et al., 1998; Moga et al., 1998).

The watershed transform is the method of choice and widely used for medical image segmentation. It is classified as a region-based segmentation method and an important field in mathematical morphology. It can provide a hierarchical image segmentation from which a single region or set of regions can be extracted *a priori* by using a threshold or interactively with the help of a graphical user interface (Kim et al., 2007). To study the physical or physiological properties for each group of pixels in a medical image, a hierarchical image segmentation is important because it can provide a set of several segmentations at different levels of segmentation detail. The segmentations at coarser levels of detail can be produced by simple merges of regions from segmentations at finer levels of detail. A unique feature of hierarchical image segmentation is that the segmented region boundaries are maintained at the full image spatial resolution at all levels of the segmentation hierarchy.

The intuitive idea underlying the watershed transform is that of a landscape or topographic relief flooded by water. In flooding a landscape or topographic relief with water, watersheds are the dividing lines of the domains of attraction of rain falling over the region. An alternative approach is to imagine the landscape being gradually immersed in a lake, with holes pierced at the local minima. Basins (called 'catchment basins') will fill up with water starting at these local minima, and, at points where water coming from different basins would meet, dams are built. When the water level has reached the highest peak in the landscape, the process is stopped. As a result, the landscape is partitioned into regions or basins separated by dams, called watershed lines or simply watersheds. One of the difficulties with this intuitive concept is that it leaves room for various formalizations. Different watershed definitions for continuous functions can be given (Jos, 2001). Our main interest in this study is in digital images, for which there is even more freedom to define watersheds because in the discrete case, there is no unique definition of the path that a drop of water follows. This produces various algorithmic specifications and implementations. In this study, we followed Insight Image Segmentation and Registration Toolkit (ITK) (ITK, 2010) and Vincent-Soille transforms (Vincent, 1991) in digital spaces, which are now used as a fundamental step in many powerful segmentation procedures.

ITK is a cross-platform application development framework widely used for the development of image segmentation and image registration programs. ITK was developed with funding from the National Library of Medicine in the USA as an open resource of algorithms for analyzing the images of the Visible Human Project. The toolkit provides a top-down watershed algorithm that first computes a complete partition of the image into basins and subsequently finds watersheds by boundary detection. This assumes a multi-scale differentiable operator and, consequently, floating point operations in two, three, and more dimensions. The software is implemented in C++, and it is wrapped for Tcl, Python, and

Java. On the other hand, Vincent-Soille transforms, developed in early 90's, are faster and flexible with adaptations to any kind of underlying grid (different connectivities) and easily extendable to n-dimensional images and to graphs. They are appropriate to the CT images because they used an integer-sorting algorithm of the pixels in increasing order of Hounsfield values and fast breadth first scanning of the plateaus enabled by a first-in-first out type data structure. The algorithm first finds basins; then, the watersheds are the voxels not included in any basin.
Mathematically rigorous algorithmic definition of the digital watershed is presented based on the Vincent and Soille's idea. In fact, other watershed algorithms could be defined in a similar manner.

Definition: Image function Let $\mathbb{Z}$ be a set of integer and $\mathbb{D} \subseteq \mathbb{Z} \times \mathbb{Z} \equiv \mathbb{Z}^2$. Define a digital image map I: $\mathbb{D} \rightarrow \mathbb{Z}$, where $\mathbb{D}$ is the domain of the image and $I(p)$ denotes the Hounsfield value of the pixel $p \in \mathbb{D}$.

Definition: Path Let $\mathbb{G} \subseteq \mathbb{Z}^2 \times \mathbb{Z}^2$ denote the pixel grid. Define a path P of length l between two pixels p and q be an $l+1$-tuple $(p_0, p_1, \cdots, p_{l-1}, p_l)$ such that $p_0 = p$, $p_l = q$ and $\forall$ $i \in [0, l) : (p_i, p_{i+1}) \in \mathbb{G}$.

Definition: Connected A set of pixels $\mathbb{M}$ is called *connected* if and only if for every pair of pixels $p,\ q \in \mathbb{M}$ there exists a path between p and q which only passes through pixels of $\mathbb{M}$.

Definition: Connected component A *connected component* is defined as a nonempty connected set of pixels of maximal size.

Definition: Minimum A *regional minimum* (or *minimum* for short) of I at altitude h is a connected component of pixels p with $I(p) = h$ from which it is impossible to reach a point of lower altitude without having to climb.

Definition: Geodesic distance Let $\mathbb{A} \subseteq \mathbb{Z}^2$, and $a,\ b$ two points in $\mathbb{A}$. The *geodesic distance* $d_{\mathbb{A}}(a, b)$ within $\mathbb{A}$ is the minimum of the lengths of all paths from a to b in $\mathbb{A}$:
$d_{\mathbb{A}}(a, b) = \min\{l(P) : P$ path between a and b which is totally included in $\mathbb{A}\}$.

Definition: Geodesic influence zone Let $\mathbb{A} \subseteq \mathbb{Z}^2$ and contain a set $\mathbb{B}$ made of several connected components, $\mathbb{B}_1, \mathbb{B}_2, \cdots, \mathbb{B}_k$. The *geodesic influence zone* of the set $\mathbb{B}_i$ within $\mathbb{A}$ is defined as:
$iz_{\mathbb{A}}(B_i) = \{p \in \mathbb{A} \mid \forall j \in [1, \cdots, k] \setminus \{i\} :\ d_{\mathbb{A}}(p, B_i) < d_{\mathbb{A}}(p, B_j)\}$.

Definition: Skeleton by influence zones (SKIZ) Let $\mathbb{A} \subseteq \mathbb{Z}^2$. The *skeleton by influence zones* (SKIZ) of the set $\mathbb{B}_i$ within $\mathbb{A}$ is defined as a complement of the union of the geodesic influence zones of the connected components of $\mathbb{B}$:
$\mathrm{SKIZ}_{\mathbb{A}}(B) = \mathbb{A} \setminus IZ_{\mathbb{A}}(B)$ with $IZ_{\mathbb{A}}(B) = \bigcup_{i \in [1;k]} iz_{\mathbb{A}}(B_i)$.

Note that SKIZ consists of all points which are equally distant from at least two connected components. However, SKIZ does not necessarily separate the different geodesic influence zones and is often made of disconnected and thick one, meaning that a set of pixels equally distant from two connected components may be thicker than one pixel.
The key feature of the Vincent-Soille algorithm is a recursive computing from the lowest pixel value (h_{min}) to the highest one (h_{max}). To explain the recursive algorithm, we define the threshold set of I at level h as follows:

Definition: Threshold set of I at level h $\mathbb{T}_h(I) = \{p \in \mathbb{D} \mid I(p) \leq h\}$.

Let $\min_h$ denote the union of all regional minima at level h. Then, the *catchment basins and watersheds by immersion* can be defined as follows.

Definition: Catchment basins and watersheds by immersion The set of the catchment basins of the image I is equal to the set $X_{h_{max}}$ obtained after the following recursion:
(1) $X_{h_{min}} = T_{h_{min}}(I)$,
(2) $X_{h+1} = \min_{h+1} \cup IZ_{T_{h+1}(I)}(X_h), \forall h \in [h_{min}, h_{max} - 1]$.

Finally, the watersheds ($\mathbb{W}_I$) of the image I correspond to the set of the pixels of $\mathbb{D}_I$ which do not belong to any catchment basin, i.e., $\mathbb{W}_I = \mathbb{D}_I \cap (X_{h_{max}})^c$. The fact that computing X_{h+1} needs X_h expresses the sequential recursive nature of this algorithm. An example of the watershed transform on the square grid according to the immersion process is shown in Fig. 5.

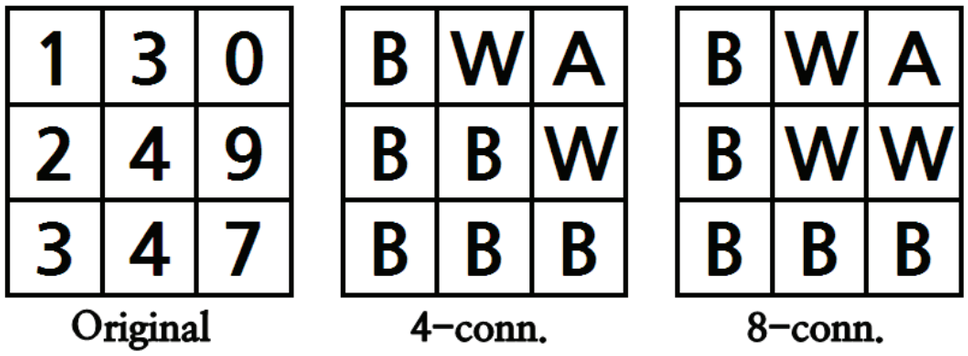

Fig. 5. Example of watershed transform. Original image is in the left-hand side, watershed with 4-connectivities in the middle, and 8-connectivities in the right-hand side.

The drawback of watershed segmentation is that it produces a region for each local minimum, resulting in oversegmentation. To alleviate this problem, a graph merging algorithm which is generally complicated, is used with a threshold value of the watershed depth, which sometimes impedes the efficient implementation of the graphical user interface. In this study, we propose an effective watershed method without a post merging process. Moreover, a steppedup graphical user interface provides a function of interactive and semi-automatic medical image segmentation.
The initial oversegmentation depends on the gradient image intensity variations because of the high sensitivity of the watershed algorithm. Thus, as a pre-processor, the noise reduction algorithm can reduce the oversegmentation appreciably. However, the image edges should be preserved to represent the boundaries of the image objects which have different physiological properties. We implemented a well-known statistical edge-preserving noise reduction algorithm. To preserve the edges, small bi-modal window filters were used. Also, the noise reduction process depends on the value of parameter of the filter size which may be user defined or can be evaluated based on the estimated noise variance. The output of the noise reduction procedure is the starting point of the gradient-based boundary sharpening process. This process is closely combined with a watershed technique, resulting in an effective watershed method without a post merging process. The gradient-based boundary sharpening technique reduces the oversegemntation by thresholding the gradient magnitude priori to

detect the watersheds of the image. To detect the boundary, a first order derivative is used in two-dimensional image:

$$\nabla I = \begin{bmatrix} G_x \\ G_y \end{bmatrix} \tag{26}$$

i_1	i_2	i_3
i_4	i_5	i_6
i_7	i_8	i_9

Fig. 6. An example of local image mask in 3×3 region.

Many different gradient operators can be used in the boundary sharpening step. Combination of the two operators also makes the edge sharper and thinner. For the mask shown in Fig. 6, the standard and cross gradient operators are given, respectively:

$$G_x = i_6 - i_5, \; G_y = i_8 - i_5, \tag{27}$$

$$G_x = i_8 - i_6, \; G_y = i_9 - i_5. \tag{28}$$

The mean value of the two gradient magnitudes results in the value of the gradient. Thresholding the gradient magnitude is performed interactively by using the graphical user interface (moving bar).

3.2 Application: Defining anatomical structures

Defining anatomical structures and the extraction of the objects in CT images are essential parts of medical imaging applications, such as diagnostic imaging, 3D treatment planning, and image-guided surgery. The volume definition process may provide for delineating the specific shape of an organ on a digital image as accurately as possible, especially for 3D rendering, radiation therapy, and surgery planning. Specifically, in the radiation treatment planning the accuracy and reproducibility of this process affects targeting, optimization based on dose-volume histograms or other volume-based measures, and the development of biological models for tumor control and complication probabilities (Kum et al., 2007).
This can be done either through manual user interactions or by applying imaging processing techniques for the automatic detection of specific structures in the image using segmentation techniques. The automatic segmentation process might involve complicated structures, and in this case usually only an expert can perform the task of identification manually on a slice-by-slice basis. Humans can perform this task using complex analyses of shape, intensity, position, texture, and proximity to surrounding structures. Thus, despite the advances in automatic segmentation methodology, many medical image research labs continue to rely on manual delineation. This reluctance to accept automation may be due to insufficient reliability and high specificity of fully automatic methods and the lack of inexpensive user-friendly tools implementing semi-automatic methods. To address this difficulty, we developed the

semi-automatic hierarchical watershed segmentation algorithms. A semiautomatic approach combines high efficiency, accuracy, and repeatability of automatic methods with expertise and quality control that can only come from human supervision.

The hierarchical watershed segmentation algorithms divide the whole medical image into many groups of pixels according to the corresponding Hounsfield values. The number of divided groups depends on the threshold value given by the user. In our current experience, a single fixed threshold has not produced adequate results, so semi-automatic human-aided adjustment is necessary. For this purpose, we have supplied a user interface with which regions can be added, replaced, or subtracted semi-automatically via the command input window in 3D and a mouse click in 2D. With a user-friendly interface tools, the watershed method is an especially elegant segmentation technique that requires the expert to provide an initialization, set control parameters, and terminate the segmentation. Moreover, it was designed to make segmentation and parameter selection as easy as possible for users without a mathematical background. The detailed pixel information for each group is included in the ASCII format output file, from which we may extract any region of interest. We found that the semiautomatic method was useful to avoid errors incurred by both human and machine sources and, in addition, provided clear and visible information for pedagogical purposes.

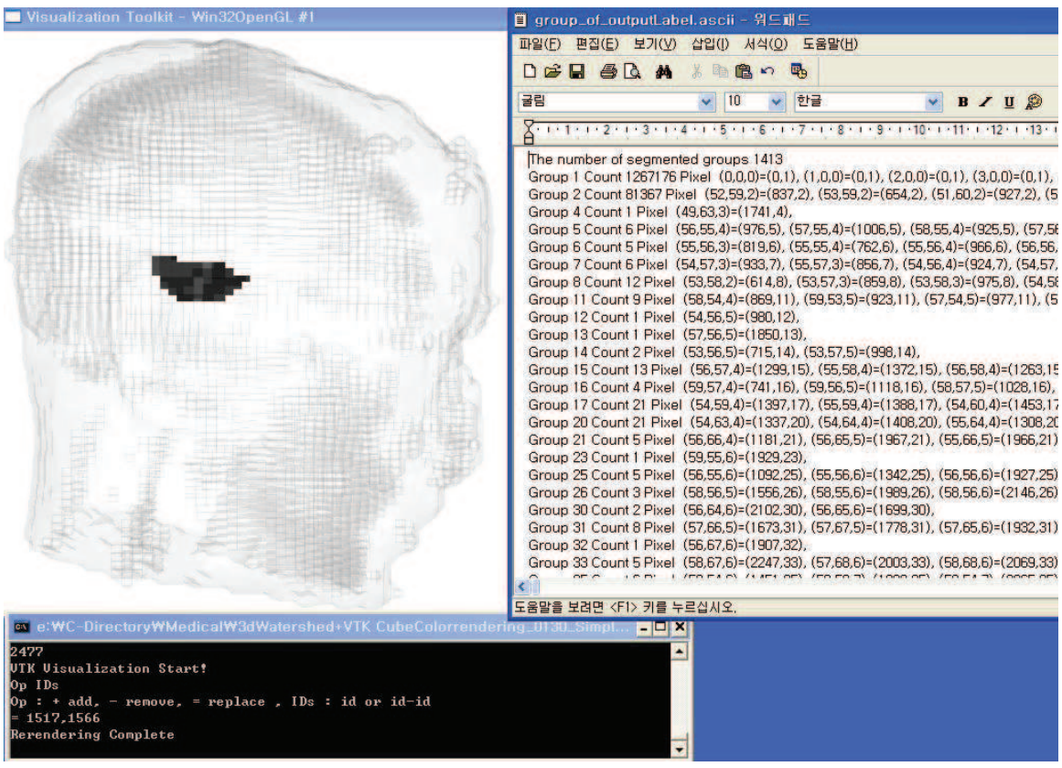

Fig. 7. Three-dimensional semi-automatic region extraction and registration procedures from the head phantom CT data.

Figure 7 shows three-dimensional semi-automatic region extraction and registration procedures from the head phantom CT data. The figure shows three windows, the three-dimensional transparent image output window with a selected volume, the ASCII file output window including group information and Hounsfield value for each pixel, and the

command input window (Kim et al., 2007). The number of segmented groups is automatically contingent on the given threshold value. It is more than just an implementation of a given computational method, which contains innovative tools for manual outlining and quality control in addition to the automatic segmentation work flow.

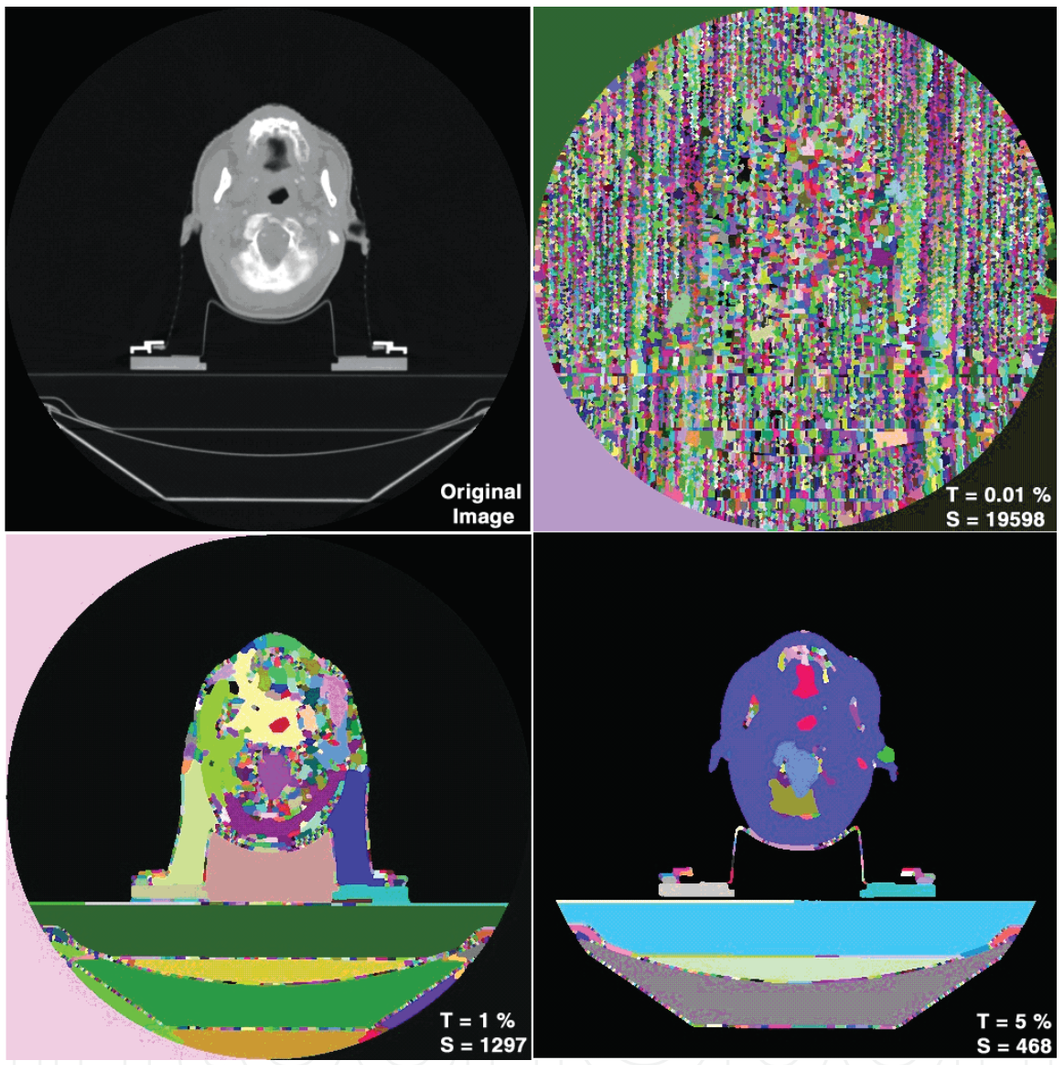

Fig. 8. Two-dimensional segmentation of the head phantom CT data.

Figure 8 shows two-dimensional segmentation of the head phantom CT data. The original CT slice is on the upper left-hand side. The threshold value is given as a percentage of maximum depth. As the threshold value (T) increases, the number of segmentations (S) decreases. This property is very useful to select a focused anatomical region automatically. A graph merging algorithm is used to adjust the number of regions. The computing time for two-dimensional problem is only a few seconds using a desktop PC. During radiation therapy, irradiating beams pass through a patient, killing both carcinoma and normal tissues. Thus, the radiation treatment must be carefully planned to deliver a clinically prescribed dose to the target volumes containing carcinoma cells, while nearby organs at risk and normal cells are

spared. To optimize the beams, we need to extract pixel numbers for each group of organs. The ASCII format output file (including group numbers and pixel addresses) is very useful to find the exact pixel numbers for the focused region.
Defining anatomical structures is an especially useful procedure for the treatment planning. The state of the art of modern treatment planning requires very tight margin and dose escalation. To meet these requirements, we obtain exact pixel addresses of the interesting anatomical regions for the calculation of an optimization matrix, whose rows represent pixel numbers and columns gantry angles, for example, in conformal 3D treatment planning. Prior to optimization, each pixel's (or voxel's) dose in the target volume and neighboring organs is calculated with respect to the gantry angle as a matrix ($d_{i,j}$), where i is the pixel address and j is the gantry angle. In general, the matrix size is too big to include all elements for the optimization. We choose a small number of pixels in the simulation, but the choice of insufficient number of pixels can cause a dose inhomogeneity problem. Frequently, we may observe hot spots that may have critical effects on the organs at risk. Thus, the pixel address information is essential for the best treatment planning. Our algorithm was developed specifically for segmenting anatomical structures and is considerably easier to master than the other packages due to its tightly focused and simple functionality.

3.3 Application: Hepatic tumor analysis

The primary goals of a CT examination of the liver are the detection and the characterization of focal hepatic lesions. The choice between surgical or palliative treatment depends on the size, number, and location of metastases as determined by the image. The detection of hepatic tumors with CT theoretically improves as lesion conspicuousness increases. Because most hepatic tumors are hypo-vascular, increased conspicuousness may be accomplished by increasing the degree of enhancement of normal surrounding liver. CT contrast agents, sometimes referred to as "dyes," are used to highlight specific areas so that the organs, blood vessels, or tissues are more visible. In this study, we show a sample patient's CT image whose liver has a comparatively large-area tumor. The results show that the use of our segmentation algorithms for studying various radiological problems, such as liver CT enhancement with contrast material, is indeed feasible. However, this is not an exhaustive radiological study for the effects of contrast materials or CT protocols (Kim et al., 2007).
Two different methods based on watershed segmentation are applied to the analysis of the hepatic tumor (see Fig. 9). The segmented images and corresponding frequency distributions of the Hounsfield values are shown in the left-hand and the right-hand columns, respectively. In each column, the four images from top to bottom represent the progressive levels of contrast materials, pre-contrast (PRE), arterial phase (ART), portal venous phase (POR), and delayed phase (DEL), respectively. Once the contrast is injected into the bloodstream, it circulates throughout the body. Advanced CT scanners with rapid acquisition times and short delay between acquisition of groups of scans permit scanning of the liver in an exclusively and separately a pre-contrast phase, an arterial phase ($\sim$ 30 sec), and a separate portal venous phase ($\sim$ 70 sec) consecutively. A couple of minutes after the portal venous phase, a delayed phase ($\sim$ 3 min in general) can be obtained. Watershed segmentation produces hierarchical region segmentations contingent on the threshold value. For the first automatic segmentation step, we adjusted the threshold values to get better segmentations, though the results were not complete. The pictures shown here were automatically segmented with the best adjusted threshold value in each phase. After this procedure, we adjusted the segmented regions semi-automatically via the command input window or mouse click.

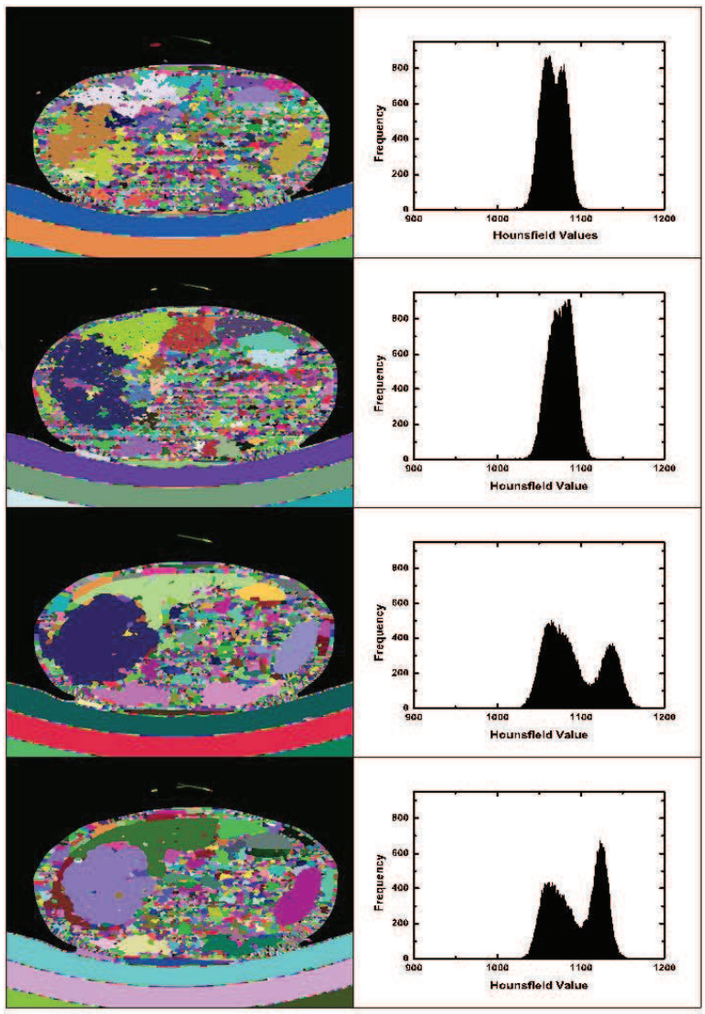

Fig. 9. Segmented images and corresponding frequency distributions of the Hounsfield values in the left-hand and the right-hand columns, respectively. In each column, the four images from top to bottom represent the progressive levels of contrast materials, pre-contrast (PRE), arterial phase (ART), portal venous phase (POR), and delayed phase (DEL), respectively.

For the appropriate region of interest chosen semi-automatically, we analyze radiological properties using regional average and median Hounsfield values, which represent X-ray transport properties.

The pre-enhanced segmented image on the top left-hand side shows many clustered regions, which are different basins in the Hounsfield values. Although there are many different basins, their average Hounsfield values are not significantly different as shown in the corresponding right-hand side histogram. Separation between tumor and normal liver is negligible, so that it is not easy to identify the hepatic tumor area from this picture. For better identification of the lesion area, it is necessary to develop augmented tools or analysis techniques. They are included in one of our on-going research activities. The segmented image of the artery phase on the left-hand side shows the focal hepatic region, although it is still not quite satisfactory.

Hepatic metastases are supplied almost exclusively by hepatic arteries, but most of these lesions are hypo-vascular and are not well visualized on images obtained during the hepatic arterial phase. On the other hand, a strongly enhanced liver lesion is readily perceived before the minimally enhanced surrounding normal liver parenchyma during the arterial phase. This result is shown clearly in the right-hand side corresponding histogram. Frequencies in tumor area are increased, compared to those of normal area. The CT's X-ray beam is weakened as it passes through the blood vessels and organs that have "taken up" the contrast. These structures are enhanced by this process and show up as white areas on the CT images. The segmented image in the third row from the top shows clearly the focal tumor region in a portal venous phase. The frequency distribution shown in the right-hand side also shows the two different groups of Hounsfield values. During the portal venous phase, the liver lesion is normally seen as a filling defect in the strongly enhanced normal liver parenchyma because approximately 70% − 75% of the hepatic parenchymal blood flow arrives from the portal vein and the remaining 25% −30% arrives from the hepatic artery (Greenway, 1971). The liver lesion, however, can be more conspicuous in either phase, depending on the vascularity of the tumor. The metastases are most conspicuous when imaging is performed with techniques that optimize portal venous enhancement, during which phase they appear as regions of low attenuation against a background of the brightly enhanced liver parenchyma. Therefore, the biggest difference in attenuation value between a liver lesion and the normal liver tissue will be visible shortly after maximum portal venous enhancement, with the lesions appearing as hypo-attenuating within a highly enhanced liver parenchyma. The length of this phase is, however, limited in time and depends on multiple parameters, among which are the volume and the rate of injection of the contrast material. Thus, the results shown in two phases (ART and POR) suggest that this patient has a hepatic metastases. The delayed phase segmented image in the bottom of the left-hand column shows clearly the focal regions. The frequency distribution in the right-hand side shows more clearly the 'V'-shape focal regions. It looks similar to the portal venous phase, which is explained by the staying time of the contrast material in the liver area. The results suggest that segmented images cannot exceed or overpower the effects of the contrast material for the liver CT scan to find the tumor area, and the histogram estimations can be used as a good measure to find tumor areas as shown in Fig. 9. However, the segmentation algorithm is useful for studying quantitative variations of the Hounsfield values in the tumor. In the histogram calculations, we used unsigned integers by adding 1000 to Eq. 4 for computational purposes so that the Hounsfield value of water is not 0 but 1000.

Segmentation is absolutely necessary to cluster Hounsfield values for each region of interest. Specifically, the semi-automatic algorithm was helpful in reducing errors incurred by both human and machine sources. The whole liver image included approximately 35000 pixels in total. Two separated peaks explain the existence of the different groups of Hounsfield values. This phenomenon explains explicitly the existence of the hepatic tumor. Frequency analysis using the segmentation algorithm shows more clearly the existence of the tumor (quantitatively) than the segmented image (qualitatively). The evidence is very clear in this sample because its tumor size is almost half of the whole liver area. It may, however, not be easy to detect a tumor from frequency analysis if the tumor size is comparatively small, but a watershed segmentation algorithm is still very helpful even for a small tumor.

Figure 10 shows the changes in the average Hounsfield values with one standard deviation as a function of the phase (PRE, ART, POR, and DEL) for both the lesion area and the normal area. In the lesion area, the mean enhancement values differed by 12, 15, 11 at the ART, the POR, and

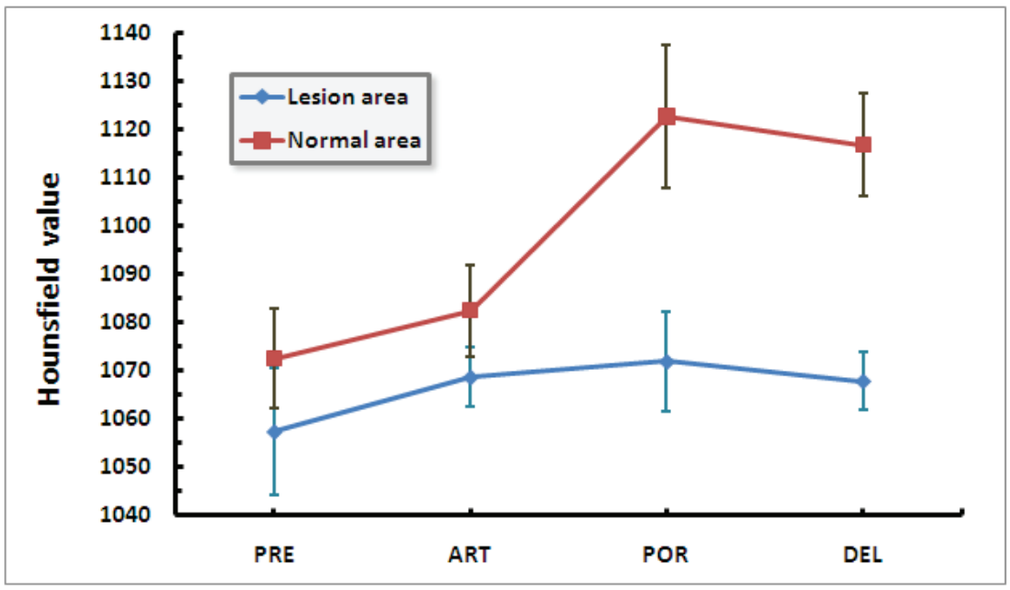

Fig. 10. Changes in the average Hounsfield values with one standard deviation as a function of the phase (PRE, ART, POR, and DEL) for both the lesion area and the normal area.

the DEL phases, respectively. On the other hand, in the normal liver region, the differences were 10, 50, 44 at the ART, the POR, and the DEL phases, respectively. Thus, in both areas, the maximum difference occurred at the POR phase. The results suggest that the liver is mostly surrounded by portal veins, and discrimination between the normal parenchyma and liver lesions is considered to be most effective in the early portal venous phase. These results also suggest that the tumor may be hepatic metastases.

Statistical analysis between different phases were performed by using t and one-way ANOVA tests for means and variances. We used the SPSS software program for the statistical analysis. The means were considered significantly different if P was less than 0.01. For each test parameter, the confidence interval was obtained by using the standard normal distributions. The statistical analysis showed that for the normal liver region, the mean Hounsfield value was 1072.4, and its standard deviation and standard error were 20.6 and 0.2, respectively. Thus, in the 95 % confidence interval, the minimum value is 1072.1, and the maximum is 1072.7. For the lesion area, the mean Hounsfield value was 1057.3 and its standard deviation and standard error were 26.1 and 0.2, respectively. This results in a minimum of 1057 and a maximum of 1058 in the 95 % confidence interval. Thus, both areas are included in the same group by Schneider et al.'s classification table (see the Table 1 in the reference) (Scheneider et al., 2000). Their densities, however, are slightly different because the density is linearly proportional to the CT number (see Fig. 7 in the same reference).

4. Analysis of radiological properties

Both the exact anatomical structures of the patient's body and quantitative information about radiological properties of the different tissues can be extracted from the CT scans as described by Eq. 2. Although the Monte Carlo simulations are the most accurate methods for radiation treatment planning, without accurate input data, they can only produce incorrect results. For the customized cancer treatment planning, each patient's physico-chemical data of the

body, such as mass density and the elemental mass fractions of the patient's tissues, is required. The Monte Carlo method for high-energy photon and charged particle transport is the most accurate for dose calculations, specifically for tissue inhomogeneities. Thus, the radiological properties relative to the beam quality used in radiotherapy planning must be obtained by conversion of the CT numbers because most CT scans are taken at X-ray energies of approximately 120 keV (fixed value).

The general approach in this direction was to divide the scale of CT numbers into different groups to correlate the CT numbers with the elemental mass fractions of the tissues, but there was no rule about how to determine the threshold values correctly. Thus, the results might, in general, depend on the therapeutic beam quality. In this direction, we used Schneider et al.'s results (Scheneider et al., 2000) to evaluate the physico-chemical properties for the normal liver and lesion areas in the first trial because they extracted the information about the tissue parameters from the CT number irrespective of the therapeutic beam quality.

However, by using the segmentation tools, we can extract different organ areas and estimate the average Hounsfields values and standard deviation from the pixels consisting of the area. Although the distribution of the CT numbers may be different for the same material (except water) due to both beam hardening effects and small machine dependent band widths, we can adjust the differences with the graphical user interface as shown in Fig. 7. For a better study, many experiments are required with the CT scanner being used for generating this CT data set. It remains as one of our on-going projects to study exhaustively the radiological properties of the patient's CT data sets. CT imaging simulations are the most efficient methods for the exhaustive study. In addition, statistical analysis for differentiating the tissues is performed as shown in hepatic tumor analysis.

Ray-tracing algorithm (used in virtual CT imaging) with Monte Carlo method may be used in the next step to optimize the treatment planning. Although the Monte Carlo method is the most accurate for dose calculations, specifically, for tissue inhomogeneities, it costly in terms of computation time in general. Therefore, deterministic calculations based on ray-tracing techniques are used as a powerful alternative to the Monte Carlo approach to optimize the treatment planning, especially with the results based on the Monte Carlo calculations, whenever computation time is a critical issue. The most popular method for the optimization is a simplex method, which is closely relevant to the optimization of the segmentation problems. Thus, a few novel computational approaches such as ray-tracing, segmentation, Monte Carlo, and optimization cover the simulations of almost all subjects ranging from CT imaging to treatment planning and quality assurance in radiotherapy. Moreover, they turned out to be all closely relevant and affect to each other in the simulations of CT imaging and its applications.

5. Conclusions

As a part of the larger numerical simulation project, "from CT imaging to customized cancer radiation treatment planning," which includes virtual X-ray imaging, image reconstruction, medical image segmentation and structure definition, radiological property analysis of the CT data, irradiating beam optimization, and scientific data visualization, we have been developing a few novel numerical approaches such as ray tracing algorithm for virtual cone beam imaging, cone beam image reconstruction algorithm, in-house general purpose Monte Carlo code (PMCEPT), semi-automatic watershed segmentation schemes to analyze CT data based on radiological and/or physical principles. In this feasibility study, we found that the Monte Carlo method was a powerful simulation approach which covered from CT imaging to

customized cancer radiation treatment planning whenever computation time is not a critical issue. However, we also found that a simpler augmented deterministic algorithm such as ray tracing was a useful alternative to the Monte Carlo approach to simulate X-ray imaging systems. The same ray tracing algorithm is also used for the fast radiotherapy treatment optimization. Moreover, a simplex optimization algorithm can be applied to optimize the image segmentation. Thus, we found that a few closely relevant numerical algorithms could be used for almost all simulations ranging from CT imaging to treatment optimization.

In this chapter, we presented some results such as the virtual X-ray imaging and reconstruction algorithms for cone beam CT, semi-automatic medical image segmentation algorithm and its applications to define anatomical structures of a head phantom CT and to analyze hepatic lesion areas with contrast material, and to calculate radiological and chemico-physical properties of the patient's liver CT data. The algorithms show outstanding performance and several characteristic features, which make it possible to apply the proposed algorithms to build a larger numerical simulation project, from CT imaging to treatment optimization. In combination with our in-house Monte Carlo code (PMCEPT code), these augmented algorithms were very useful to study CT image and its various applications. According to our experiences on this study, the algorithms are not separated but closely relevant to each other, so that the experience of an algorithm accelerates the study of other algorithms. Eventually, they can be combined into one system for studying almost all areas of CT imaging, which is one of our on-going research activities.

6. Acknowledgments

We first thank Prof. William G. Hoover for his careful proofreading and thoughtful comments. This research was supported by Basic Science Research Program through the National Research Foundation of Korea(NRF) funded by the Ministry of Education, Science and Technology(grant number: 2010-0003983).

7. References

Colijn, A., & Beekman, F. (2004). Accelerated simulation of cone beam X-ray scatter projections. *IEEE Transections on Medical Imaging*, Vol.23, No. 5, pp 584-590. May, 2004.

Cullen, D., Hubbell, J., & Kissel, L. (1997). EPDL97: The evaluated photon data library '97 Version. *UCRL-LR-50400*, Vol.6, Rev 5., Sept. 1997.

Duvauchelle, P., Freud, N., Valérie, K., & Babot, D. (2000). A computer code to simulate X-ray imaging techniques. *Nuclear Instruments and Methods in Physics Research B*, Vol.170, pp 245-258. 2000.

Freud, N., Duvauchelle, P., Létang, J., & Babot, D. (2006). Fast and robust ray casting algorithms for virtual X-ray imaging. *Nuclear Instruments and Methods in Physics Research B*, Vol.248, pp 175-180. 2006.

Freud, N., Duvauchelle, P., Pistrui-Maximean, S., Létang, J., & Babot, D. (2004). Deterministic simulation of first-order scattering in virtual X-ray imaging. *Nuclear Instruments and Methods in Physics Research B*, Vol.222, pp 285-300. Jan, 2004.

Feldkamp, L., Davis, L., & Kress, J. (1984). Practical cone-beam algorithm. *J. Opt. Soc. Am. A*, Vol.1, No. 6, pp 612-619. June 1984.

Greenway, C., & Stark, R. (1971). Hepatic vascular bed. *Physiol. Rev.*, Vol.51, No. 1, PP 23-65. Jan. 1971.

Gu, L., Xu, J., & Peters, M. (2006). Novel multistage three-dimensional medical image segmentation: Methodology and validation. *IEEE Transactions on Information Technology in Biomedicine*, Vol. 10, No. 4, PP 740-748. Oct. 2006.

Haris, K., Efstratiadis, S., Maglaveras, N., & Katsaggelos, A. (1998). Hybrid image segmentation using watersheds and fast region merging. *IEEE Transactions on Image Processing*, Vol. 7, No. 12, PP 1684-1699. 1998.

ITK-homepage, www.itk.org.

Roerdink, J., & Meijster, A. (2001). The watershed transform: Definitions, algorithms and parallelization strategies. *Fundamenta Informaticae*, Vol. 41, PP 187-228. 2001.

Ju, S., Han, Y., Kum, O., Cheong, K., Shin, E., Shin, J., Kim, J. & Ahn, Y. (2010). Comparison of film dosimetry techniques used for quality assurance of intensity modulated radiation therapy. *Med. Phys.*, Vol.37, No.6, pp 2925-2933. June, 2010.

Kak A., & Slaney, M. (1999). *Principles of Computerized Tomographic Imaging.* IEEE Press, The Institute of Electrical and Electronics Engineers, Inc., New York. ISBN 0-87942-198-3.

Kum, O. (2010). *Medical Statistics with Monte Carlo Methods.* Jinhan M&B Press, Seoul, Korea. ISBN 978-89-8432-471-8.

Kum, O. & Park, K. (2010). *Biomedical Engineering.* Jinhan M&B Press, Seoul, Korea. ISBN 978-89-8432-446-6.

Kum, O., Kim, H., & Max, N. (2007). Semi-automatic watershed medical image segmentation methods for customized cancer radiation treatment planning simulation. *Int. J. CARS*, Vol.2, (Suppl) No.1, pp S44-S45. June, 2007.

Kim, H., Kum, O., & Max, N. (2007). Computer-aided CT image analysis aased on clustered Hounsfield values. *J. Korean Phys. Soc.*, Vol.51, No.1, pp 235-244. July, 2007.

Kum, O., & Kim H. (2007). Semi-automatic segmentation of CT image using watershed algorithm and graphical user interface (abstract). *Med. Phys.*, Vol.34, No.6, pp 2394-2394. June, 2007.

Kum, O. (2007). Telematics-based online client.server/client collaborative environment for radiotherapy planning simulations. *Med. Bio. ENg. Comput.*, Vol.45, No.11, pp 1053-1063. November, 2007.

Kum, O., Lee H., Kim, J., Song T., Park K., & Han, Y. (2007). Simpler and faster watershed medical image segmentation algorithm (abstract). *Med. Phys.*, Vol.35, No.6, pp 2663-2663. June, 2008.

Kum, O.,& Lee, S. (2005). Development of a parallel electron and photon transport code (PMCEPT) I: Method and absorbed dose computation in water. *J. Korean Phys. Soc.*, Vol.47, No.4, pp 716-725. October, 2005.

Kim, H.,& Kum, O. (2006). Development of a parallel electron and photon transport (PMCEPT) code II: Absorbed dose computation in homogeneous and heterogeneous media. *J. Korean Phys. Soc.*, Vol.49, No.4, pp 1640-1651. October, 2006.

Kum, O., Park, K., & Han, Y. (2009). Semantic web-based PMCEPT Monte Carlo code simulations in medical physics. *J. Korean Phys. Soc.*, Vol.55, No.5, pp 2242-2247. November, 2009.

Lagravére, M., Carey, J., Ben-Zvi, M., Packota, G., & Major, P. (2008). Effect of object location on the density measurement and Hounsfield conversion in a NewTom 3G cone beam computed tomography unit. *Dentomaxillofacial Radiology*, Vol.37, pp 305-308., 2008.

Li, N., Zhao, H., Cho, S., Choi, J., & Kim, M. (2008). A fast algorithm for voxel-based deterministic simulation of X-ray imaging. *Computer Physics Communications*, Vol.178, pp 518-523. Jan. 2008.

Miceli, A., Thierry, R., Flisch, A., Sennhauser, U., Casali, F., & Simon, M. (2007). Monte Carlo simulations of a high-resolution X-ray CT system for industrial applications. *Nuclear Instruments and Methods in Physics Research A*, Vol.583, pp 313-323. Sept., 2007.

Moga, A., Cramariuc, B., & Gabbouj, M. (1998). Parallel watershed transformation algorithms for image segmentation. *Parallel Computing*, Vol. 24, PP 1981-2001. 1998.

Moore, C., Amer, A., Marchant, T., Sykes, J., Davies, J., Stratford, J., McCarthy, C., MacBain, C., Henry, A., Price, P., & Williams, P. (2006). Developments in and experience of kilovoltage X-ray cone beam image-guided radiotherapy. *The British Journal of Radiology*, Vol.79, pp S66-S78. Jan., 2006.

Peterzol, A., Létang, J., & Babot, D. (2008). A beam stop based correction procedure for high spatial frequency scatter in industrial cone-beam X-ray CT. *Nuclear Instruments and Methods in Physics Research B*, Vol.266, pp 4042-4054. July, 2008.

Scheneider, W., Bortfeld, T., & Schlegel, W. (2000). Correlation between CT numbers and tissue parameters needed for Monte Carlo simulations of clinical dose distributions. *Phys. Med. Biol.*, Vol. 45, PP 459-478. 2000.

Siddon, R. (2010). Fast calculation of the exact radiological path for a three-dimensional CT array. *Med. Phys.* Vol.12, No.2, pp. 252-255, Mar/Apr 1985.

Vincent, L., & Soille, P. (1991). Watersheds in digital spaces: An efficient algorithm based on immersion simulations. *IEEE Transactions on Pattern Analysis and Machine Intelligence*, Vol. 13, NO. 6, PP 583-598. 1991.

Wang, G., Lin, T., Cheng, P., & Shinozaki, D. (1993). A general cone-beam reconstruction algorithm. *IEEE Transactions on Medical Imaging*, Vol.12, No. 3, pp 486-496. Sept. 1993.

Zhao, X., Hu, J., & Zhang, P. (2009). GPU-based 3D cone-beam CT image reconstruction for large data volume. *International Journal of Biomedical Imaging*, Vol.2009, Article ID 149079, pp 1-8. June 2009.

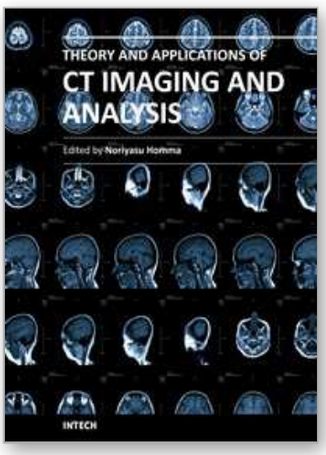

Theory and Applications of CT Imaging and Analysis
Edited by Prof. Noriyasu Homma

ISBN 978-953-307-234-0
Hard cover, 290 pages
Publisher InTech
Published online 04, April, 2011
Published in print edition April, 2011

The x-ray computed tomography (CT) is well known as a useful imaging method and thus CT images have continuingly been used for many applications, especially in medical fields. This book discloses recent advances and new ideas in theories and applications for CT imaging and its analysis. The 16 chapters selected in this book cover not only the major topics of CT imaging and analysis in medical fields, but also some advanced applications for forensic and industrial purposes. These chapters propose state-of-the-art approaches and cutting-edge research results.

How to reference
In order to correctly reference this scholarly work, feel free to copy and paste the following:

Oyeon Kum (2011). Novel Computational Approaches for Understanding Computed Tomography (CT) Images and Their Applications, Theory and Applications of CT Imaging and Analysis, Prof. Noriyasu Homma (Ed.), ISBN: 978-953-307-234-0, InTech, Available from: http://www.intechopen.com/books/theory-and-applications-of-ct-imaging-and-analysis/novel-computational-approaches-for-understanding-computed-tomography-ct-images-and-their-application

INTECH
open science | open minds

InTech Europe
University Campus STeP Ri
Slavka Krautzeka 83/A
51000 Rijeka, Croatia
Phone: +385 (51) 770 447
Fax: +385 (51) 686 166
www.intechopen.com

InTech China
Unit 405, Office Block, Hotel Equatorial Shanghai
No.65, Yan An Road (West), Shanghai, 200040, China
中国上海市延安西路65号上海国际贵都大饭店办公楼405单元
Phone: +86-21-62489820
Fax: +86-21-62489821

IntechOpen